Earth and Planetary Science Letters 594 (2022) 117713

Contents lists available at ScienceDirect

Earth and Planetary Science Letters

www.elsevier.com/locate/epsl

Boulder exhumation and segregation by impacts on rubble-pile asteroids

J. Ormö [a,*], S.D. Raducan [b], M. Jutzi [b], M.I. Herreros [a,c], R. Luther [d], G.S. Collins [e], K. Wünnemann [d,f], M. Mora-Rueda [a,c], C. Hamann [d]

[a] Centro de Astrobiología CSIC-INTA, Instituto Nacional de Técnica Aeroespacial, 28850 Torrejón de Ardoz, Spain
[b] Space Research and Planetary Sciences, Physikalisches Institut, University of Bern, Bern, Switzerland
[c] Departamento de Ingeniería Térmica y Fluidos, Universidad Carlos III de Madrid, 28911 Leganés, Spain
[d] Museum für Naturkunde, Leibniz-Institut für Evolutions- und Biodiversitätsforschung, Berlin, Germany
[e] Department of Earth Science & Engineering, Imperial College, London, UK
[f] Freie Universität Berlin, Institute of Geological Sciences, Berlin, Germany

ARTICLE INFO

Article history:
Received 16 December 2021
Received in revised form 23 June 2022
Accepted 4 July 2022
Available online 21 July 2022
Editor: W.B. McKinnon

Keywords:
impact cratering
rubble-pile asteroids

ABSTRACT

Small asteroids are often considered to be rubble-pile objects, and such asteroids may be the most likely type of Near Earth Objects (NEOs) to pose a threat to Earth. However, impact cratering on such bodies is complex and not yet understood. We perform three low-velocity (≈ 400 m/s) impact experiments in granular targets with and without projectile-size boulders. We conducted SPH simulations that closely reproduced the impact experiments.

Our results suggest that cratering on heterogeneous targets displaces and ejects boulders, rather than fragmenting them, unless directly hit. We also see indications that as long as the energy required to disrupt the boulder is small compared to the kinetic energy of the impact, the disruption of boulders directly hit by the projectile may have minimal effect on the crater size.

The presence of boulders within the target causes ejecta curtains with higher ejection angles compared to homogeneous targets. At the same time, there is a segregation of the fine ejecta from the boulders, resulting in boulders landing at larger distances than the surrounding fine grained material. However, boulders located in the target near the maximum extent of the expanding excavation cavity are merely exhumed and distributed radially around the crater rim, forming ring patterns similar to the ones observed on asteroids Itokawa, Ryugu and Bennu. Altogether, on rubble-pile asteroids this process will redistribute boulders and finer-grained material heterogeneously, both areally around the crater and vertically in the regolith. In the context of a kinetic impactor on a rubble-pile asteroid and the DART mission, our results indicate that the presence of boulders will reduce the momentum transfer compared to a homogeneous, fine-grained target.

1. Introduction

The fraction of the asteroid population that has survived since Solar System formation has experienced numerous collisional, dynamical, and thermal events, which have shaped their structures and orbital properties. As a result, small such asteroids are often considered to be rubble-pile objects: aggregates held together by self-gravity or small cohesive forces (Richardson et al., 2002; Sánchez and Scheeres, 2014). Rubble-pile asteroids may be the most likely type of Near Earth Objects (NEO) to pose a threat to Earth in a future collision event (Popova et al., 2011). A better understanding of cratering processes on heterogeneous, rubble-pile like targets would therefore aid interpretation of the collisional history of small Solar System bodies as well as efforts to design effective asteroid deflection technology.

NASA's Double Asteroid Redirection Test (DART) is the first space mission to test the controlled deflection of a near-Earth asteroid, the secondary of the 65803 Didymos asteroid system, Dimorphos. The DART spacecraft will impact the small moon and alter its orbital period around the primary, by a measurable amount (Cheng et al., 2018). ESA's Hera mission (Michel et al., 2018) will arrive at Dimorphos a few years after the DART impact and provide a detailed characterization of the impact outcome, including

* Corresponding author.
E-mail address: ormoj@cab.inta-csic.es (J. Ormö).

https://doi.org/10.1016/j.epsl.2022.117713

the morphometry and morphology of the DART impact crater. Both of the Didymos system components, the 780 m main asteroid and the 160 m moon, Dimorphos, are assumed to be rubble-pile objects that have separated due to the spin initiated by the YORP effect (e.g., Rozitis et al., 2014; Zhang et al., 2021).

Rubble-pile asteroids are thought to be composed of blocks (boulders) up to tens of meters in size embedded in finer material. The presence of large boulders may affect the crater morphology, as is apparent on the relatively well-studied asteroids Bennu (e.g., Lauretta et al., 2019; Walsh et al., 2019) investigated by NASA's OSIRIS-REx mission and Ryugu, explored by JAXA's Hayabusa2 mission (e.g., Arakawa et al., 2020; Cho et al., 2021). Studies of craters on the rubble-pile asteroid Ryugu, for example, show that abundant boulders on and under the surface have affected crater morphology (Cho et al., 2021). On this asteroid, craters typically have relatively large boulders remaining on the rim forming a circular pattern outlining the crater. Likewise, large craters (diameter >100 m) host abundant and sometimes relatively large boulders on their floors compared with the crater size, whereas small craters (<20 m) are characterized by smooth floors with relatively few boulders compared with the exterior.

Cho et al. (2021) suggest that the intra-crater boulders in the larger craters were exposed by preferential excavation of finer material, similar to what was observed for the SCI impact experiment (Small Carry-on Impactor; Arakawa et al., 2020). However, at the smaller craters the crater-forming impact merely removes boulders on or near the surface, which leads to exposure of finer materials just below the near-surface boulders. The SCI impacted a boulder-rich area on Ryugu, and produced a crater approximately 15 m in diameter (Arakawa et al., 2020), causing boulder movement in the close proximity to the crater.

Recent impact experiments and numerical studies (e.g., Housen and Holsapple, 2011; Jutzi and Michel, 2014; Luther et al., 2018; Raducan et al., 2019) have shown that the ejection behavior and the resulting kinetic impact deflection efficiency depend strongly on the target properties and structure, and are non-unique (i.e., the same spacecraft impact onto asteroids with different target properties can result in the same deflection (Raducan et al., 2020)). For an unambiguous interpretation of the DART impact outcome, therefore, it is imperative to measure both the impact deflection efficiency (often referred to in terms of β, where β represents the change in momentum of the asteroid/impactor momentum) and the crater size and morphology, to help infer the target properties of the asteroid independently. In addition, it is important to understand the influence of asteroid properties on the cratering process, including the effect of target heterogeneities. For this reason, laboratory scale experiments and rigorously validated impact simulation software, so-called shock physics codes, are essential to predict asteroid deflection by a kinetic impactor.

A number of previous impact experiments have studied impact cratering in granular media involving projectiles larger than the target grain size (e.g., Cintala et al., 1999), granular media involving projectiles of similar size with the target grain size (e.g., Barnouin-Jha et al., 2005; Güttler et al., 2012; Tatsumi and Sugita, 2018), or granular media involving projectiles much smaller than the target grain size or heterogeneity (e.g., Durda et al., 2011). We are only aware of one study where impact cratering was investigated in granular media with projectile-sized embedded objects, which are more similar to asteroid surfaces: Housen and Holsapple (2014) performed a set of preliminary experiments at the NASA Ames Vertical Gun Range into targets with grain sizes about the same as the projectile, or larger. In one experiment they used a 50/50 random blend of roughly projectile-size grains and clasts with diameters about ten times that of the projectile. The target was suspended with springs of known strength so that the momentum transfer and, thus, β could be calculated.

Housen and Holsapple (2014) compared their deflection results with results from similar experiments into both homogeneous and heterogeneous targets of various grain sizes (e.g., Holsapple and Housen, 2012). They concluded that β is fairly insensitive to the size of the rubble-pile constituents, even when they are nearly an order of magnitude larger than the impactor. However, the experiment with the 50/50 mixed target produced a β value that was higher than for all the various homogeneous grain size targets. Nevertheless, it was not certain what the reason for the larger β value was. Thus, the influence of heterogeneous granular targets on cratering remains poorly understood despite its important implications for the cratering on rubble-pile asteroids.

Here we present new impact experiments into targets specifically designed to mimic rubble-pile asteroid surfaces, with projectile-size, porous boulders (ceramic balls) embedded in a fine-grained matrix (beach sand). One target configuration considers a scenario with a relatively homogeneous distribution of boulders, whereas a second scenario applies a distinct lateral change in the boulder distribution. A third scenario, with a homogeneous target of the same sand as used as matrix between the ceramic balls, serves as reference. We investigate the effect on crater formation, material ejection, and the final crater morphology. The results are used for the validation of numerical simulations carried out in concert with the experiments.

2. Methodology

2.1. Impact experiments

The impact experiments were conducted at the Experimental Projectile Impact Chamber (EPIC) at Centro de Astrobiología CSIC-INTA, Spain (Fig. 1A). The design, capacities, and procedures for target and gun preparations of the EPIC, as well as reproducibility of results, are described in detail by Ormö et al. (2015). The main component of the EPIC is the compressed-gas gun that can launch 20 mm in diameter projectiles at velocities up to approximately 420 m/s and at varied impact angles. In this study, we used spherical projectiles of Delrin, which is a micro-crystalline polymer of high strength, hardness, and rigidity that disrupts upon impact at the velocities and target properties used in this study. Ormö et al. (2015) concluded that Delrin projectiles are well suited for dry sand targets. They also showed that repeated shots with the EPIC gun into granular targets have high reproducibility (less than 10% difference) and scale consistently with impact craters in the hypervelocity regime both in the laboratory and in nature. These tests suggest that the uncertainty introduced by the experiment set-up is very small. The experiments included in our current study follow the same experimental methodology.

The experiments were recorded with a NAC Memrecam GX-8 with a resolution of 800 × 600 pixels when set at a frame rate of 5000 fps and the, for these experiments necessary, recording time (approximately 2.5 s). The target was illuminated by five Fotodiox PRO LED100WB-56 Studio LED High-Intensity Daylight lamps.

We carried out three quarter-space experiments (cf. Piekutowski, 1980; Ormö et al., 2015) with different target set-ups: Experiment 1 – a complete target of ceramic balls embedded in beach sand (Fig. 1B–D); Experiment 2 – half the target consisted of ceramic balls embedded in beach sand and the other half was pure beach sand (Fig. 1E–F); and Experiment 3 – a completely homogeneous target of pure beach sand as a reference.

The properties of the target beach sand are described in Ormö et al. (2015). Grain size data were measured at Centro de Astrobiología CSIC-INTA by standard sieving technique. Friction angle and density were measured at the Boeing laboratory in Seattle (for details see Ormö et al., 2015). The beach sand was in all cases applied as "slow pour" to achieve maximum compaction (cf. Ormö et

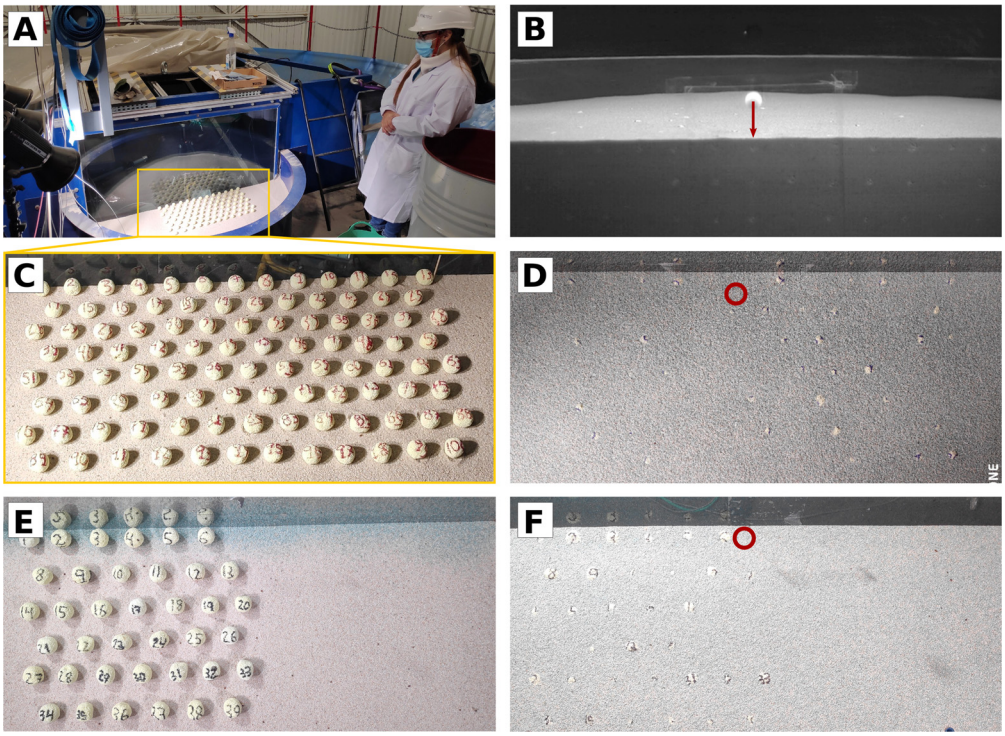

Fig. 1. The Experimental Projectile Impact Chamber (A) The target set-up for Experiment 1 (complete rubble-pile target). (B) Front view through the camera tank window (5 cm thick to eliminate vibrations) showing the projectile (at beginning of the arrow) just before impact and the embedded layers of ceramic balls ("boulders") for quarter-space Experiment 1. The point of impact is at the end of the red arrow. (C) Top view during preparations for Experiment 1: Four layers of porous ceramic balls were positioned directly on top of each other, with one ball-diameter spacing between each ball in x, y and z directions. The uppermost layer was just barely covered by sand (D, top view). The red circle indicates the point of impact, which was at the flank of ball 7 in the row next to the window. (E) Top view of the target set-up for Experiment 2 (half `rubble-pile', half homogeneous sand target). The photo shows the ball distribution of the topmost layer out of three layers. The distance and relative positions between balls are the same as in Experiment 1. Likewise, the top layer was then just barely covered by sand (F, top view). The red circle indicates the impact point. To study the coupling between the projectile and the sand target, there was no ball placed at the impact point (cf. Experiment 1). (For interpretation of the colors in the figure(s), the reader is referred to the web version of this article.)

al., 2015; Housen et al., 2018), with a density of 1.8 g/cm^3 and a friction angle of 34.6°. Physicochemical properties of the ceramic balls such as dimensions, mass, density, porosity, and chemical composition were measured at the Centro de Astrobiología CSIC-INTA, and the micro X-ray fluorescence laboratory at Museum für Naturkunde Berlin (for methodology and details see Suppl. Material 1).

The porous ceramic balls, hereafter called "boulders", are approximately 2.25 cm in diameter, have an estimated unconfined compressive strength of ≈1 MPa, and a porosity of about 66%. Notwithstanding differences in chemical composition, the ceramic material of the balls is considered to be a good mechanical analogue for the boulders found on the rubble-pile asteroids Ryugu and Bennu (cf. Ballouz et al., 2020). The balls were chosen because they have a diameter and density similar to the projectiles. For more details on the target materials see Table 1. All targets were covered by a thin layer (<1.5 mm) of colored sand in order to facilitate the analysis of ejecta emplacement.

This is a qualitative study of the effects of boulder inclusions in the target. The setup is complex and time consuming and it was not possible to apply a quantitative approach. Therefore, we must rely on the high reproducibility of similar EPIC experiments mentioned above. Nevertheless, there are several additional parameters that we would have liked to have varied but could not because of the said limitations, e.g., spacing between boulders, irregular vs. regular distribution, variable and different boulder size. The extensive experimental effort allowed more systematic studies using numerical methods (see section 2.2); however, further numerical modeling of the experiments are very demanding in terms of computational resources and are beyond the scope of this paper.

2.2. Numerical model

To further study the impact scenarios described above, we used Bern's grid-free smoothed-particle hydrodynamics (SPH) shock physics code (Jutzi et al., 2008; Jutzi, 2015) to reproduce the EPIC impact experiments. SPH is well suited to model high velocity impacts on heterogeneous asteroids. The code includes material models relevant for geological materials, various equations of state and a porosity compaction model, the P-α model (Jutzi et al., 2008).

The granular target matrix was modeled using a Tillotson EoS for SiO_2 (adapted from Melosh, 2007) and a Drucker-Prager rheology, with a coefficient of internal friction of $f = 0.56$. The initial porosity of the target matrix was kept constant at ≈30% and was modeled using the P-α model, with a simple quadratic crush curve (Jutzi et al., 2008) defined by the solid pressure, $P_s = 0.2$ GPa, elastic pressure, $P_e = 1$ MPa, transition pressure, $P_t = 0.2$ GPa, transition distension, $\alpha_t = 1$, exponents $n_1 = 2$ and $n_2 = 2$, and initial distension, $\alpha_0 = 1.48$. The full description of the P-α model implemented in the Bern SPH code is given by Jutzi et al. (2008). The choice of crush curve parameters was informed by the experimental crush curve data for Lane Mtn. 20/30 sand (Housen et al., 2018). The boulders were modeled using a Tillotson EoS for SiO_2, and a tensile strength and fracture model as described in (Jutzi, 2015), with parameters corresponding to a tensile strength of $Y_T \approx 1$ MPa. The porosity of the boulders was set to match the size, mass and bulk density of the boulders, and was modeled using the nominal parameters $P_s = 0.1$ GPa, $P_e = 1$ MPa, $P_t = 0.1$ GPa, $\alpha_t = 1$, $n_1 = 2$, $n_2 = 2$ and $\alpha_0 = 2.0$.

The target was modeled as a half-sphere, with a radius of 28 cm, and was made of 6 million SPH particles. Due to the very

Table 1
Projectile and target details for the EPIC impact experiments.

	Projectile	Boulders	Experiment 1 (rubble-pile)	Experiment 2 (half rubble-pile)	Experiment 3 (homogeneous)
Material	Delrin	Ceramic	Beach sand* + full target ceramic boulders	Beach sand* + half target ceramic boulders	Beach sand*
Diameter, d	20 mm	22.5 ± 1.6 mm	–	–	0.25-1 mm (grain size)
Mass, m	5.7 g	5.7 ±0.5 g	–	–	–
Density, ρ_0	1.36 g/cm^2	≈0.96 g/cm^3	–	–	1.8 g/cm^3
Porosity, ϕ_0	–	≈66%	≈32% (sand) + ≈66% (boulders)	≈32% (sand) + ≈66% (boulders)	≈32%
Impact velocity, U	–	–	397 m/s	380 m/s	405 m/s

*For details see Ormö et al. (2015). The sand porosity was calculated based on given mineral composition and densities.

Table 2
Inputs for the SPH impact simulations.

Description	Delrin impactor	Ceramic boulders	Beach sand
Material	Delrin[a]	SiO_2[b]	SiO_2[b]
Equation of state	Mie Gruniesen	Tillotson	Tillotson
Strength model	Hydrodynamic	Tensile[c]	Drucker-Prager
Initial bulk modulus, A (GPa)	7.52	35.9	35.9
Drucker-Prager strength parameters			
Cohesion, Y (Pa)	–	–	0.1
Strength at infinite pressure, Y_{lim} (GPa)	–	–	0.1
Internal friction coefficient, f	–	–	0.56

[a] Ormö et al. (2015).
[b] Melosh (2007).
[c] Jutzi (2015).

Table 3
EPIC experiments results.

	Experiment 1 (rubble-pile)	Experiment 2 (half rubble-pile)	Experiment 3 (homogeneous)
Transient crater diameter, D_{TC}	17.3 cm	19.3 cm (Equal radius on both sides)	21.4 cm
Transient crater depth, h_{TC}	2.9 cm	2.6 cm (sand side) 2.9 cm (rubble-pile side)	2.5 cm
Transient crater growth time, T_{TC}	40 +/−5 ms	65 +/−5 ms Same for both sides	70 +/−5 ms
Final crater diameter, D_{FC}	20.4 cm	21.2 cm (Equal radius on both sides)	22.5 cm
Final crater depth, h_{FC}	2.9 cm	2.6 cm (sand side) 2.9 cm (rubble-pile side)	2.5 cm

Diameters and depths are relative to the target surface.

long crater growth times, the EPIC experiments described above are very computationally expensive to replicate with SPH. To ensure numerical stability, the maximum simulation time-step, dt, is limited by the Courant criteria (e.g., Anderson, 1987), which for the simulations of the EPIC experiments means that the maximum time-step must be: $dt < \text{resolution}/c_s \approx 10^{-7}$ s, where c_s is the sound speed in the target. However, the ejecta and boulder reaccumulation occurs after a few hundred ms. To model the entire process with SPH, therefore, we switch to a so-called "fast time integration scheme" in the shock physics code calculation at the time $t_{transition} = 30$ ms, after the transient crater is formed. At this time, the initial shock and fragmentation phase is over and the late-stage evolution is governed by low-velocity granular flow. This allows us to artificially change the material properties of the target to a low sound-speed (c_s) medium allowing for a larger timestep. This "fast integration scheme" was described in detail in Raducan and Jutzi (2022). In this phase of the calculation, we apply for all materials a simplified Tillotson EoS, in which all energy related terms are set to zero. The remaining leading term of the EoS is governed by the bulk modulus $P = A(\rho/\rho_0 - 1)$, which also determines the magnitude of the sound speed. We use $A \approx 1$ MPa and also reduce the shear modulus proportionally. The SPH input parameters are summarized in Table 2.

3. Results

3.1. Crater growth and the transient crater

Visualizations and details on the development of the craters in the three experiments are given in Suppl. Material 2. Crater excavation in Experiment 1 begins with a symmetric bowl-shaped cavity, similar to the homogeneous target Experiment 3, and the growing crater retains this shape until the maximum depth is reached (cf. Melosh, 1989). Analysis of high-speed video footage shows that after the maximum depth is reached the lateral expansion continues until T ≈ 40 ms, when a "kink" develops in the ejecta curtain (Fig. 4A). The emergence of this kink marks the end of excavation. After this time the excavation flow inside the crater has ceased and the ejecta curtain travels away from the crater cavity depositing near-field ejecta behind it to form the crater rim. In the gravity regime, the crater cavity stops growing when the residual kinetic energy is insufficient to displace the target against its own weight.

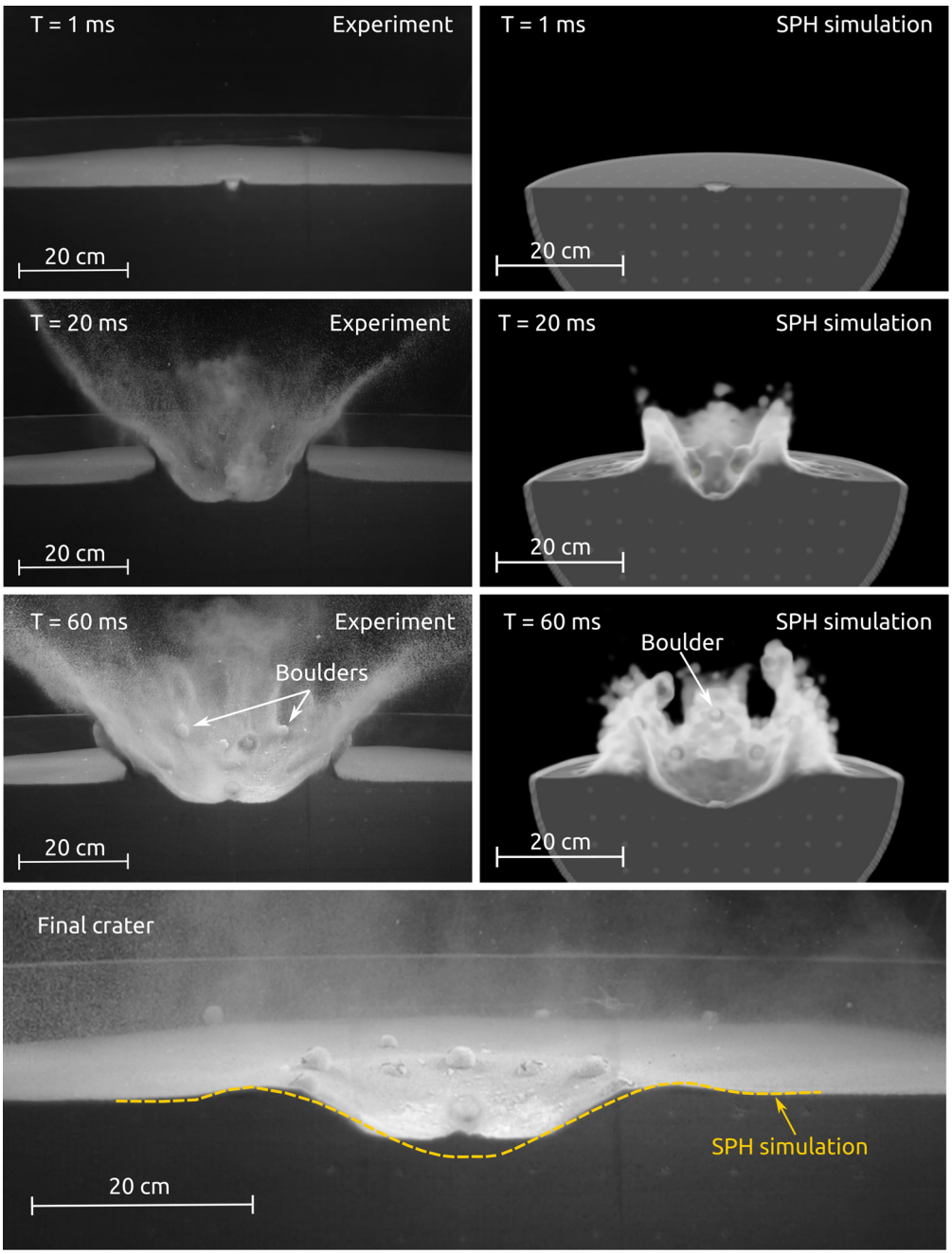

Fig. 2. Time evolution of Experiment 1 (rubble-pile target). In the experiment, only boulders from the topmost layer participated in the cratering to any noticeable degree. The boulder at the impact point was crushed, the boulders next in line outwards were ejected at lower angles than the sand ejecta curtain, causing them to pass through the curtain and land about 0.6 m from their original positions. The rest of the boulders spanned by the growing crater were displaced to positions on top of the crater rim. The boulder in layer two just below the crushed boulder was displaced 0.5 cm downwards. Both the transient and the final crater had a relatively steeper wall than the reference crater in homogeneous sand (see Experiments 3, Fig. 5). Except for a slightly shallower crater in the experiment, the SPH simulation shows a good fit in crater dimensions and shape. Please note that the fast SPH ejecta are not displayed in the simulation (see section 3.3).

Thus, in the experiments, the moment when the ejecta curtain starts to bend over the forming crater rim, creating the observed kink, defines the time of transient crater formation (T_{TC}). This time should correspond to the moment of maximum crater volume; however some uncertainty from the definition of the ejecta kink in the video frames is present (Table 3). The crater rim formation can be seen until $T \approx 60$ ms, after which the ejecta curtain continues to move across the surface and the ejecta and boulders are deposited on the target surface by $T \approx 300$ ms.

During the lateral expansion of the crater prior to T_{TC}, the cavity becomes relatively flat-floored and steep-walled (Fig. 2). The crater in the numerical simulation, on the other hand, maintains a deeper, more bowl-shaped profile, albeit with a relatively steep crater wall. This is likely due, at least in part, to the relatively low spatial resolution employed which results in a relatively thick ejecta curtain as well as visualization artifacts (e.g., material around the crater rim is diffuse and has lower density yet it is visualized as an opaque material). It may also be due to a deficiency in the material model used to describe the behavior of the sand. Nevertheless, the fit of the final crater profile between experiment and simulation is good.

The earliest stage of crater excavation in Experiment 2 is similar to that observed in Experiment 1 (Fig. 3). However, later excavation is clearly affected by the absence of boulders on one side

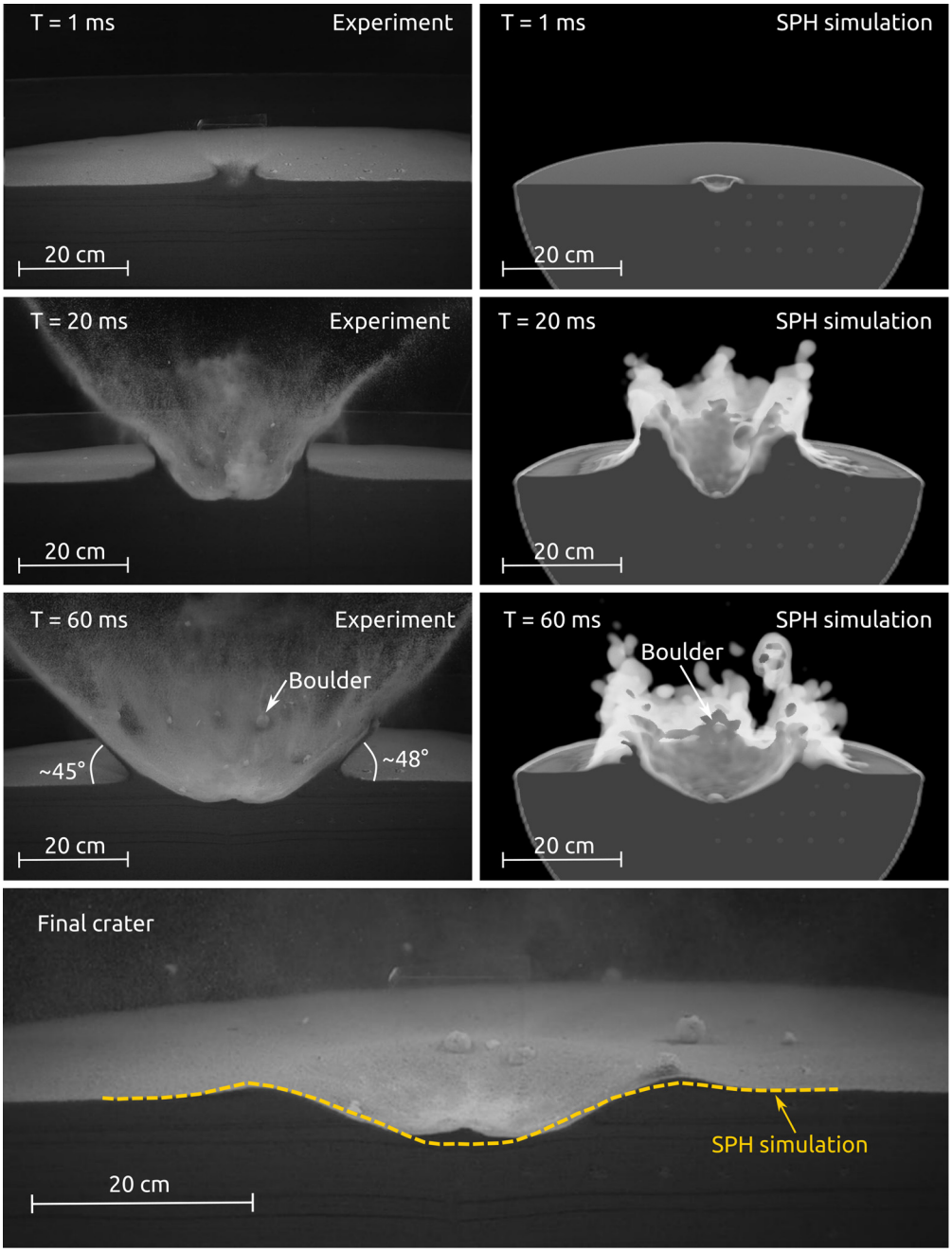

Fig. 3. Time evolution of Experiment 2 ("half" rubble-pile target). In this experiment, there was no boulder directly at the point of impact. However, it had negligible effect on the excavation and the boulder ejection, which followed an identical pattern as that of Experiment 1 (Figs. 2, 5). In the time frame 60 ms (just before the transient crater reached its maximum dimension), it is apparent that the wall of the sand-side part of the crater (left) is shallower, and with lower ejecta curtain angle, than for the rubble-pile side (right). Except for a slight 'hump' on the floor of the experiment crater, the SPH simulation shows a good fit in crater dimensions and shape. Layers of colored sand in the experiment target (dark horizontal lines) show the displacement of the sand within the target. Please note that the fast SPH ejecta are not displayed in the simulation (see section 3.3).

of the target. On the side of the target with boulders, cavity expansion follows that of Experiment 1, whereas on the side with homogeneous sand the cavity obtains a shallow bowl-shape with a lower wall slope angle, as well as lower ejecta curtain angle similar to that of Experiment 3. Nevertheless, there is no noticeable difference in the emergence of the kink in the ejecta curtain (T_{TC}) between the two halves of the crater (Table 3). However, the transient crater is reached at different times for the full rubble-pile target (Experiment 1) compared with the other two, which may be considered equal in time (Table 3).

When the transient crater shape of the two rubble-pile experiments is compared with that of the homogeneous sand target in Experiment 3 (Fig. 4A; Suppl. Mtrl. 2), it is noticeable that the existence of boulders in the target affects the crater growth. In Experiment 1 and 2 the crater wall and ejecta curtain angles are steeper than in the homogeneous sand target (Experiment 3). The transient crater formed in Experiment 1 (rubble-pile target) is 16% deeper, but almost 20% smaller in diameter than the equivalent Experiment 3 crater in homogeneous sand. The Experiment 2 crater in the half-and-half target, as expected, falls in between the Experiment 1 and Experiment 3 craters. The transient crater dimensions are summarized in Table 3. Seven repeated shots by Ormö et al. (2015) in homogeneous sand targets show an error of 10% in the transient and final crater-diameters, and 5% in their depths, all fac-

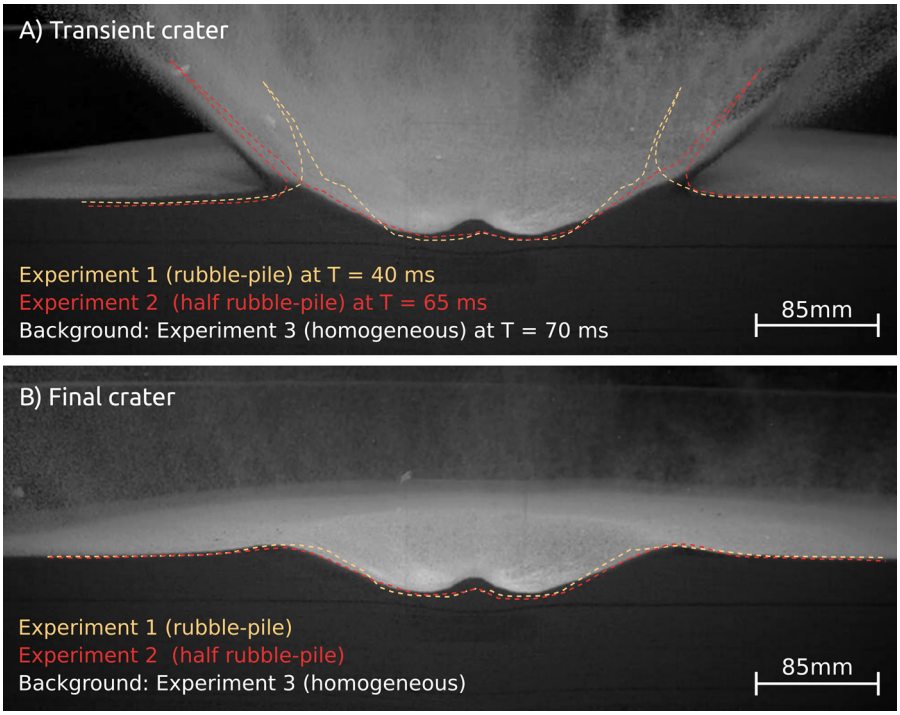

Fig. 4. Transient and final crater morphologies. (A) Transient crater profiles of Experiments 1 and 2 overlaid over the transient crater of Experiment 3 formed in a homogeneous sand target. This transient stage of the crater development is determined when a "kink" is visible in the angle of the ejecta curtain just after it has detached from the crater cavity to form the crater rim. The crater in the sand-target part of Experiment 2 (left hand side) fits to the Experiment 3 crater (background), whereas the rubble-pile part of Experiment 2 (right hand side) fits to the smaller and more steep-walled rubble-pile crater in Experiment 1. (B) Final crater profiles from Experiment 1 and Experiment 2 overlaid over the final crater from Experiment 3. A layer of colored sand (dark horizontal line) shows the slight displacement of the sand within the target.

tors kept equal. Therefore, we consider the observed differences between our three experiments to be significant.

3.2. Final crater size and morphology

The observed size difference in transient crater dimensions between the rubble-pile target in Experiment 1 and the homogeneous sand target in Experiment 3 remains to some extent also for the final craters (Fig. 4B) although the difference in crater diameter decreases to only about 10%. However, there is no change in crater depth between the transient and final craters. An analysis of the high-speed videos indicates a slight collapse of the initially steeper transient crater wall, especially for the craters formed in targets with embedded boulders.

3.3. Impact ejecta distribution

Figs. 5A–C show the crater profiles, including the ejecta curtain, from the three experiments, at three different times ($T = 20$, 60 and 80 ms). Our experiments show that the presence of the boulders within the target (i.e., Experiment 1 and the right half of Experiment 2) results in a steeper ejection angle and hence a few degrees steeper ejecta curtain compared to a homogeneous target scenario (Experiment 3).

Our SPH simulations show good agreement with the experiments in terms of the crater growth and final crater size (Figs. 2, 3). For the visualization of the simulation data, the SPH kernel interpolation is used to compute the continuum density distribution. Using this visualization approach, the fast ejecta (represented by a relatively small number of SPH particles) are not fully resolved and are therefore not visible. However, the underlying mass-velocity distribution of the SPH particles can be used to investigate quantitatively the differences in the ejecta mass-velocity distribution between the three impact scenarios. Figs. 5D–F show the cumulative mass fraction of the ejecta material that is ejected at speeds higher than v/U, where U is the projectile speed, at three different times ($T = 20$, 60 and 80 ms). The data from the SPH simulations show that there is more mass ejected at a given time in the homogeneous target case, compared to the two rubble-pile cases. This result suggests that the presence of the boulders within the target inhibits the ejection process at certain velocities.

We integrated the ejecta mass velocity-distribution to determine the cumulative, vertically ejected momentum $p_{ej(z)}/mU = (\beta - 1)$, as a function of ejection speed in the vertical direction vz, at $T = 20$, 60 and 80 ms (Fig. 5G–I). The differences seen in the ejecta mass-velocity distributions between the homogeneous target (Experiment 3) and the rubble-pile targets (Experiments 1 and 2) are also present in the ejecta momentum distribution, suggesting that the boulders also inhibit the vertically ejected momentum.

3.4. Boulder ejection and redistribution

The process of boulder ejection in Experiments 1 and 2 is complex and the boulder's fate depends on where in the excavation zone they were initially placed (Fig. 6A). In Experiment 1, the boulder below the impact point was crushed to dust. During the initial stage of the crater formation (induced by the initial shock wave propagation), there is a 0.5 cm downwards displacement of the boulder closest to the impact point in the layer below, but no other boulder displacement is visible. In Experiment 2, the absence of the boulder at the impact point seems not to affect the boulder ejection behavior. A comparison between the final crater morphology (Fig. 4B) and boulder redistribution (Fig. 6B) shows that the boulders in the fully rubble-pile target of Experiment 1 and those of the rubble-pile half of the target in Experiment 2 have nearly identical behavior during displacement and ejection.

Boulders that were initially placed in the top layer of the target well within the transient crater were excavated with the rest of the sand matrix (Fig. 6A). In both experiments only boulders from

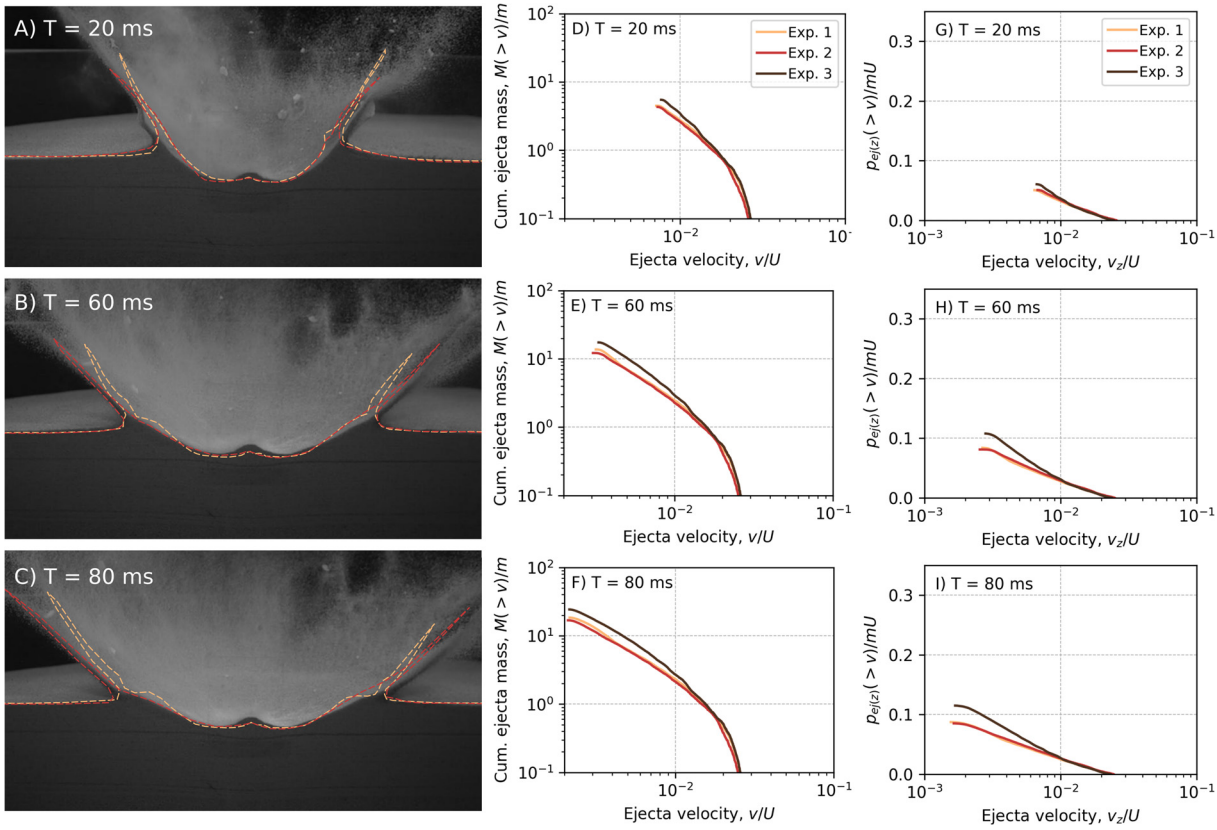

Fig. 5. (Left) Crater and ejecta profile from Experiments 1 and 2, overlaid over the Experiment 3 crater, at (A) T = 20 ms, (B) T = 60 ms and (C) T = 80 ms. (Middle) Cumulative mass of ejected particles at speeds greater than v, as a function of normalized ejection speed v/U, from the SPH simulations of the three experiment, at (D) T = 20 ms, (E) T = 60 ms and (F) T = 80 ms. (Right) Cumulative momentum of ejected particles at speeds greater than v_z, as a function of normalized vertical ejection velocity, v_z/U, at (G) T = 20 ms, (H) T = 60 ms and (I) T = 80 ms.

the top layer were excavated. Fig. 6A (left) shows a schematic representation of the crater excavation and displaced zones.

The boulders remained entrained within the ejecta curtain until they reached an altitude of about a few cm above the pre-impact target level. Here, the boulders become separated from the ejecta curtain and pierce through the ejecta cone (see Figs. 2 and 3), acquiring a 'topspin' (i.e., forward rotation over the top) at the same time. The observed trajectories of the ejected boulders suggest that after detaching from the rest of the ejecta curtain, the boulders have lower ejection angles compared to the finer sand material ejected from similar target positions relative to the impact point. As a result, these boulders land at a greater distance than the continuous sand ejecta layer, i.e., approximately 60 cm from their original positions (see Suppl. Mtrl. 2). Even though these experiments were carried out in the presence of the Earth atmosphere, the difference in the observed trajectories of the boulders and the fine ejecta is not consistent with atmospheric effects, suggesting that a different mechanism (e.g., interaction with the sand particles in the ejecta curtain) is responsible for the boulder and fine ejecta detachment.

The passage of the boulders through the ejecta curtain creates transient holes in the sand ejecta curtain (see Suppl. Mtrl. 2). The presence of boulders also results in the focusing of fine sand ejecta into streams that follow the boulders and produce crater rays (Fig. 6B). The effect of embedded objects on ejecta ray formation has also been studied by Kadono et al. (2019).

The boulders located at a distance of about three boulder diameters from the impact point (and initially close to the transient crater cavity wall) were exhumed and uplifted onto the crater rim (Fig. 6A, right), None of the ejected or displaced boulders show any visible damage. Fig. 6B shows the final boulder configuration around the crater. The boulder movements were well reproduced by the numerical simulation.

4. Discussion

4.1. Experiments and numerical simulations

Two of the most conspicuous differences between the part of the experimental craters formed in rubble-pile targets and the part formed in homogeneous sand are the sand matrix ejection angle and focusing of ejecta into rays. The ejection angle is generated by the interplay of pressure gradients (from the radially expanding shock wave, the gradient towards the free surface and the release wave). The ejected boulders behave like one particle, but on much larger scales compared to the sand grains, which means that the boulders on the surface are mobilized later than the surrounding fine material. As a result, the boulders induce a fine-material flow around them, which causes the steeper ejection angle of the fine material (i.e., the sand) and the ejecta rays.

In our experiments 1 and 2 and numerical simulations we observe only a small effect on crater dimensions whether or not there was a boulder at the impact point. Nevertheless, there is a small, but noticeable, difference (1 cm) in transient crater radius between Experiment 1 and the boulder-side of the crater in Experiment 2 (Table 3, Fig. 4A), and a more significant difference in T_{TC} (Table 3). To investigate if these differences could be due to the crushing of the porous boulder in Experiment 1, we can calculate the energy required to disrupt the boulder: According to previous studies, the specific impact energy threshold for catastrophic disruption at the boulder size scale is around 1e3-1e4 J/kg (e.g., Jutzi et al., 2010). Assuming a mass of the boulders of around 5 g, this

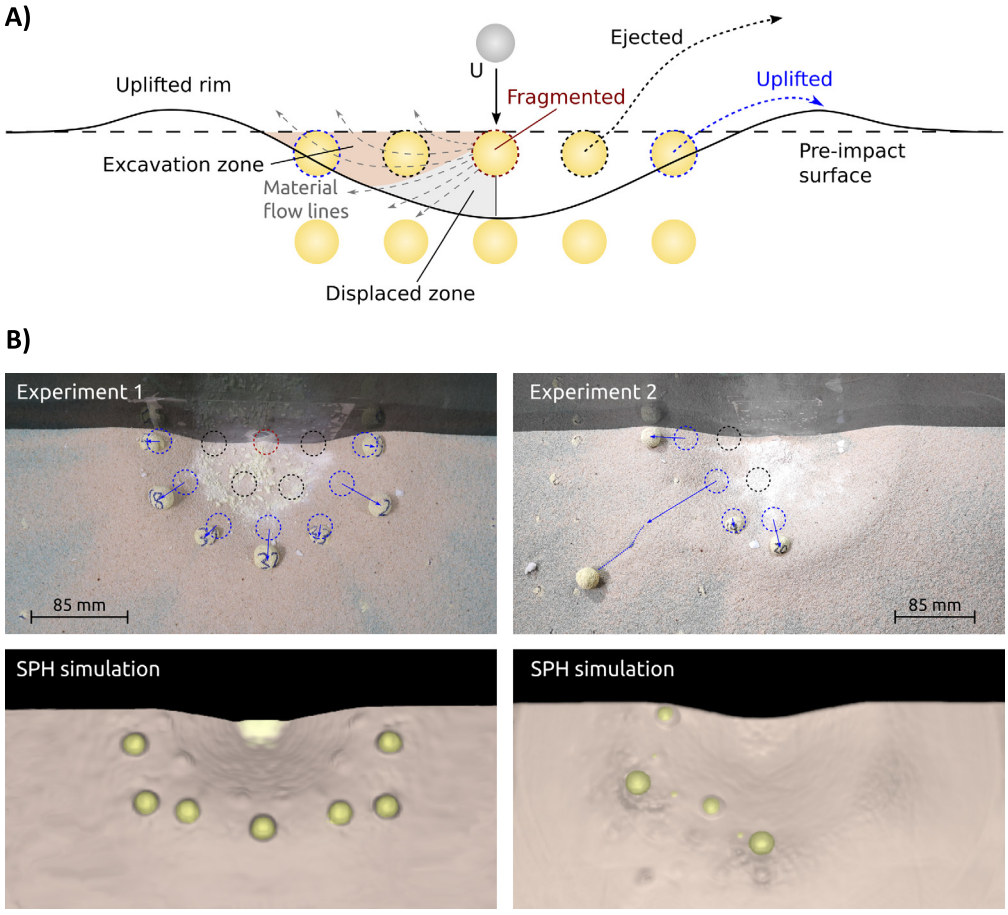

Fig. 6. A) Schematic representation of the crater excavation mechanism. The projectile impacts the target at a velocity U and fragments the boulder placed at the impact point. The shock waves and the subsequent rarefaction waves set the material into motion, in the direction of the material flow lines. The material in the excavation zone (orange) is ejected beyond the crater rim, while the material in the displaced zone (gray) is displaced and does not reach the surface. The boulders close to the transient crater cavity are uplifted to the crater rim. B) Final boulder configuration around the crater. The dotted circles show the initial position of the boulders. The impactor and the boulder placed at the point of impact (red dotted circle) were fragmented (Experiment 1), while the boulders placed in immediate proximity to the impact point (black dotted circles) remained intact but were ejected to distances of about 0.6 m. Experiment 2 did not have a boulder at the impact point. Boulders placed more than three boulder diameters away from the impact point (blue dotted circles) also remained intact and were displaced towards the crater rim. The SPH simulations were able to closely reproduce these observations. The sand ejecta were focused into rays at significantly greater extent in Experiment 1 and the rubble-pile side of Experiment 2 than in the homogeneous sand target-half of Experiment 2 and in Experiment 3. (For interpretation of the colors in the figure(s), the reader is referred to the web version of this article.)

gives an energy of <50 J needed for disruption. While this value is not an upper limit of the energy needed to pulverize the boulder, it is very small compared to the kinetic energy of the impact, which is around 449 J (397 m/s impact velocity and 5.7 g projectile mass). However, we also note that the initial kinetic energy in Experiment 1 was slightly ($\sim$37 J) higher than in Experiment 2. Therefore, we can say that there is a difference between the experiments (most noticeable in the T_{TC}), but we cannot exactly quantify to what extent this is an effect of the boulder crushing.

The reason for the different T_{TC} between Experiment 1 and Experiments 2 and 3 may be due to a combination of factors: Firstly, there is a higher amount of sand in Experiments 2 (the sand side) and 3, compared to Experiment 1, which may result in slightly different bulk properties (i.e., effective friction) of the targets; Secondly, the relationship between T_{TC} and the crater size is non-linear (i.e., a large difference in T_{TC} corresponds to a rather small difference in the crater size (Schmidt and Housen, 1987)); Thirdly, the coupling to the target may be affected by the presence of the boulder at the impact point, albeit as we show above, it may have only a small effect on the crater size. Lastly, part of the difference in T_{TC} can also be attributed to the errors associated with the measured T_{TC} (Table 3).

Our results suggest that impacts on heterogeneous targets similar to the ones investigated in our study produce the displacement of boulders, rather than fragmentation, except for the boulders directly hit by the projectile. Similar results were obtained by Housen and Holsapple (2014) for their 5 km/s impact experiments into coarse gravel. Our results are also in line with the recent SCI impact on Ryugu that displaced several boulders on the asteroid surface (Arakawa et al., 2020).

The small 'hump' at the center of the craters, most notably in Experiment 3, is not a central peak known from natural complex craters (e.g., Melosh, 1989 and references therein) nor is it a 'central mound' due to target layering (cf. Quaide and Oberbeck, 1968; Raducan et al., 2020). This effect was seen previously in other impact and half-buried explosion experiments into compacted granular targets (e.g., Piekutowski, 1977; Mizutani et al., 1983; Schultz and Gault, 1985). We are currently investigating its formation in both quarter-space and half-space target configurations. Preliminary results show that target configuration (e.g., quarter space vs. half-space, rubble-pile vs. homogeneous) is not a factor. Our preferred explanation is that it is an effect of the relatively higher effective compressive strength of densely packed sand grains (i.e., the "slow pour" sand used here, cf. Ormö et al., 2015). Densely packed sand is harder to compress downward than to shear outward, compared to a loosely packed sand, which provides less resistance to downward flow. Recent impact experiments in sands of different compaction (Cline and Cintala, 2022) investigated the

formation of these humps in more detail and they concluded that the humps might be a consequence of greater shear strengths in granular materials with high coefficients of static friction. Nevertheless, the formation of this small central feature is considered of no significance to the current study.

Previously, impact experiments into coarse-grained targets studied the "armouring effects" (e.g., Tatsumi and Sugita, 2018), where the cratering efficiency is reduced due to the energy dissipation at the collision site. It is important to note that armouring effects do not always occur for projectile-to-target grain-size ratios lower than 1 (e.g., Fig. 17 in Tatsumi and Sugita, 2018). The ratio between the projectile kinetic energy to the energy required to disrupt the larger clast in the target is more important than the projectile to grain size ratio (Housen and Holsapple, 2014). Moreover, in our experiments the boulders are loosely packed and are embedded in a much finer granular medium, placing these impact experiments in a different regime facilitating the crater growth compared to the experiments conducted by Tatsumi and Sugita (2018).

4.2. Consequences for impacts on rubble-pile asteroids

On asteroid surfaces we expect to find a wide size-distribution of grains and boulders (e.g., from mm to m sized boulders; DellaGiustina et al., 2019; Michikami et al., 2019). An impactor at the average impact velocity in the main asteroid belt catastrophically disrupts a surface grain more than 20 times its own size (Tatsumi and Sugita, 2018). Consequently, only very large surface boulders (larger than a few meters) may affect the craters made by meter-size impactors.

Our results suggest that a large proportion of the craters we see on asteroids might not have been influenced by armouring effects, and the classical crater scaling (e.g., Holsapple and Schmidt, 1987) still applies. Consequently, the age estimations for rubble-pile asteroids, based on these scaling laws, might also be valid. The boulder size-frequency distribution was not varied in our experiments, however, it may be an important factor when determining the impact outcome.

In our experiments, boulders within close proximity of the impact point are ejected at angles close to $\sim 45^{o}$, lower than the sand matrix and, thus, land at a relatively larger distance. This suggests that impacts on rubble-pile asteroids will redistribute boulders and finer-grained material heterogeneously, potentially resulting in segregation of boulders from fine-grained material.

Moreover, boulders that were initially positioned close to the edge of the transient crater are exhumed onto the crater rim. The ejection and exhumation of boulders in the excavation zone results in a depletion of boulders between the pre-impact surface and the maximum depth of excavation. Recent observations of the surface morphologies on Ryugu and Bennu observed textural differences between the interior of the craters and their exterior. Craters about $\sim$10 m in diameter generally have smoother interiors than the surrounding and compared to larger, $>$100 m craters. Cho et al. (2021) attributed this textural difference to the presence of a subsurface layer, about 2 m thick, of fine grained material.

Our laboratory and numerical results are consistent with these observations and we propose that this observed vertical boulder size sorting is produced by impact cratering. Small impacts (which are also the most numerous) exhume the boulders within the excavation zone and produce a segregation of fine material from the boulders.

Boulders much more massive than the projectile will probably remain on the crater floor, as seen in the case of the SCI impact (Arakawa et al., 2020). Moreover, an increase in kinetic energy would expose deeper located boulders within the target. However, due to the current experimental set-up limitations (i.e., maximum projectile diameter and velocity was applied), this could not be investigated.

The quasi-circular distribution of boulders along the crater rim, observed in this study, is consistent with observations of craters at Ryugu (cf. Cho et al., 2021). Similarly, some craters on asteroid Itokawa have smooth floors and concentrically distributed boulders (e.g., Hirata et al., 2009). The accumulation of relatively large boulders on crater rims is also known from much larger impact craters, for instance on the Moon and Earth (Melosh, 1989, fig. 6.1).

Another main consequence of the presence of the boulders within the target is a change in crater ejecta morphology. The boulders in our simulations caused a steeper ejecta cone compared to a homogeneous target impact, as well as distinct ejecta rays. Similarly, in the SCI impact, the south side of the crater was obscured by a large $\approx$5 m boulder and the ejecta cone was separated into four rays of material, as opposed to a continuous uniform ejecta curtain observed for homogeneous targets.

In the context of the DART mission, it is likely that the presence of the boulders on, and within, the asteroid surface will affect the ejecta cone and, ultimately, the mass-velocity distribution of the ejecta (similar to the experiments and numerical results presented here) and the momentum transfer efficiency.

While the momentum transfer efficiency, β, was not directly measured in the experiments, the results from our SPH suggest that for the targets investigated here, the presence of the boulders causes a lower β. However, ejected boulders from the asteroid's surface, which will depend on the initial boulder configuration on the surface, will also drastically affect our current understanding of asteroid deflection by a kinetic impactor. Future numerical studies with the Bern SPH code will need to investigate in more detail the effects of boulders on Dimorphos, at the scale of the DART impact.

5. Conclusions

Crater formation on a rubble-pile like target is a complex process, which involves fragmentation, ejection and displacement of boulders. We used the EPIC facility at CAB CSIC-INTA, Spain, to perform three low-velocity ($\approx$ 400 m/s) impact experiments in granular targets with and without projectile-scale boulders. We considered three different target configurations: a granular sand target with boulders embedded in the target at regular intervals across the entire target and with a boulder being disrupted at the impact point, a similar configuration but with boulders only embedded across half of the target and with no boulder at the impact point, and a homogeneous sand target. We conducted SPH simulations that closely reproduced the impact experiments.

Our experimental and simulation results suggest that, at least for the impact conditions applied here, cratering on heterogeneous targets displaces and ejects boulders, rather than fragmenting them, except for any boulders directly hit by the projectile. In such cases, we see indications that as long as the energy required to disrupt the boulder is small compared to the kinetic energy of the impact, the disruption of boulders directly hit by the projectile has minimal effect on the crater size.

On the other hand, the presence of boulders in the target noticeably affects target excavation and ejection. Impacts into the rubble-pile target produced ejecta with higher ejection angles compared to the homogeneous sand target. Boulders well within the transient crater are ejected at lower angles ($\sim 45^{o}$) than the sand matrix and, thus, land at a relatively larger distance. This suggests that impacts on rubble-pile asteroids will redistribute boulders and finer-grained material heterogeneously, potentially resulting in segregation of boulders from fine-grained material.

Simulation data also indicates that a greater mass is ejected at higher velocities in the homogeneous target scenario compared to the rubble-pile targets, which results in more momentum in the

ejected material. In the context of a kinetic impactor on a rubble-pile asteroid and the DART mission, it is likely that the presence of boulders will reduce the momentum transfer compared to a homogeneous, fine-grained target.

Our impact experiments and simulations show that boulders embedded just below the surface, inside the crater and near the crater rim are exhumed and distributed radially around the crater rim. Similar patterns have been observed around craters on rubble-pile asteroid surfaces, such as Itokawa, Ryugu and Bennu. Our experiments serve as a useful validation exercise for impact codes and can aid in the interpretation of impact craters seen on rubble-pile asteroids.

CRediT authorship contribution statement

J. Ormö: Conceptualization, Data curation, Formal analysis, Funding acquisition, Investigation, Methodology, Project administration, Resources, Supervision, Validation, Visualization, Writing – original draft, Writing – review & editing. **S.D. Raducan:** Conceptualization, Formal analysis, Methodology, Software, Validation, Visualization, Writing – original draft, Writing – review & editing. **M. Jutzi:** Conceptualization, Formal analysis, Methodology, Writing – review & editing. **M.I. Herreros:** Conceptualization, Formal analysis, Investigation, Methodology, Validation, Visualization, Writing – original draft, Writing – review & editing. **R. Luther:** Conceptualization, Investigation, Software, Validation, Writing – review & editing. **G.S. Collins:** Conceptualization, Writing – review & editing. **K. Wünnemann:** Conceptualization, Writing – review & editing. **M. Mora-Rueda:** Formal analysis, Investigation, Validation. **C. Hamann:** Data curation, Investigation, Visualization, Writing – review & editing.

Declaration of competing interest

The authors declare that they have no known competing financial interests or personal relationships that could have appeared to influence the work reported in this paper.

Acknowledgements

JO and MIH were supported by the Spanish State Research Agency (AEI) Project No. MDM-2017-0737 Unidad de Excelencia "María de Maeztu" – Centro de Astrobiología (CSIC-INTA) and the CSIC I-LINK project LINKA20203. They are also grateful for all support provided by Instituto Nacional de Técnica Aeroespacial. SDR, MJ, RL and KW have received funding from the European Union's Horizon 2020 research and innovation programme under grant agreement No. 870377 (NEO-MAPP). GSC was funded by UK Science and Technology Facilities Council Grant (ST/S000615/1).

Appendix A. Supplementary material

Supplementary material related to this article can be found online at https://doi.org/10.1016/j.epsl.2022.117713.

References

Anderson, C.E., 1987. An overview of the theory of hydrocodes. Int. J. Impact Eng. 5, 33–59.

Arakawa, M., Saiki, T., Wada, K., Ogawa, K., Kadono, T., Shirai, K., Sawada, H., Ishibashi, K., Honda, R., Sakatani, N., Iijima, Y., Okamoto, C., Yano, H., Takagi, Y., Hayakawa, M., Michel, P., Jutzi, M., Shimaki, Y., Kimura, S., Mimasu, Y., Toda, T., Imamura, H., Nakazawa, S., Hayakawa, H., Sugita, S., Morota, T., Kameda, S., Tatsumi, E., Cho, Y., Yoshioka, K., Yokota, Y., Matsuoka, M., Yamada, M., Kouyama, T., Honda, C., Tsuda, Y., Watanabe, S., Yoshikawa, M., Tanaka, S., Terui, F., Kikuchi, S., Yamaguchi, T., Ogawa, N., Ono, G., Yoshikawa, K., Takahashi, T., Takei, Y., Fujii, A., Takeuchi, H., Yamamoto, Y., Okada, T., Hirose, C., Hosoda, S., Mori, O., Shimada, T., Soldini, S., Tsukizaki, R., Iwata, T., Ozaki, M., Abe, M., Namiki, N., Kitazato, K., Tachibana, S., Ikeda, H., Hirata, N., Hirata, N., Noguchi, R., Miura, A., 2020. An artificial impact on the asteroid (162173) Ryugu formed a crater in the gravity-dominated regime. Science 368, 67–71.

Ballouz, R.-L., Walsh, K.J., Barnouin, O.S., DellaGiustina, D.N., Asad, M.A., Jawin, E.R., Daly, M.G., Bottke, W.F., Michel, P., Avdellidou, C., Delbo, M., Daly, R.T., Asphaug, E., Bennett, C.A., Bierhaus, E.B., Connolly, H.C., Golish, D.R., Molaro, J.L., Nolan, M.C., Pajola, M., Rizk, B., Schwartz, S.R., Trang, D., Wolner, C.W.V., Lauretta, D.S., 2020. Bennu's near-Earth lifetime of 1.75 million years inferred from craters on its boulders. Nature, 1–5.

Barnouin-Jha, O.S., Cintala, M.J., Crawford, D.A., 2005. Impact into coarse grained spheres. In: Mackwell, S., Stansbery, E. (Eds.), Lunar and Planetary Inst. Technical Report, 36th Annual Lunar and Planetary Science Conference, vol. 36, p. 1585.

Cheng, A.F., Rivkin, A.S., Michel, P., Atchison, J., Barnouin, O., Benner, L., Chabot, N.L., Ernst, C., Fahnestock, E.G., Kueppers, M., Pravec, P., Rainey, E., Richardson, D.C., Stickle, A.M., Thomas, C., 2018. AIDA DART asteroid deflection test: planetary defense and science objectives. Planet. Space Sci. 157, 104–115.

Cho, Y., Morota, T., Kanamaru, M., Takaki, N., Yumoto, K., Ernst, C.M., Hirabayashi, M., Barnouin, O.S., Tatsumi, E., Otto, K.A., Schmitz, N., Wagner, R.J., Jaumann, R., Miyamoto, H., Kikuchi, H., Hemmi, R., Honda, R., Kameda, S., Yokota, Y., Kouyama, T., Suzuki, H., Yamada, M., Sakatani, N., Honda, C., Hayakawa, M., Yoshioka, K., Matsuoka, M., Michikami, T., Hirata, N., Sawada, H., Ogawa, K., Sugita, S., 2021. Geologic history and crater morphology of asteroid (162173) Ryugu. J. Geophys. Res., Planets 126 (8), e2020JE006572.

Cintala, M.J., Berthoud, L., Hörz, F., 1999. Ejection-velocity distributions from impacts into coarse-grained sand. Meteorit. Planet. Sci. 34 (4), 605–623.

Cline II, C.J., Cintala, M.J., 2022. The effects of target density, porosity, and friction on impact crater morphometry: exploratory experimentation using various granular materials. Meteorit. Planet. Sci., 1–19.

DellaGiustina, D.N., Emery, J.P., Golish, D.R., Rozitis, B., Bennett, C.A., Burke, K.N., Ballouz, R.-L., Becker, K.J., Christensen, P.R., Drouet d Aubigny, C.Y., Hamilton, V.E., Reuter, D.C., Rizk, B., Simon, A.A., Asphaug, E., Bandfield, J.L., Barnouin, O.S., Barucci, M.A., Bierhaus, E.B., Binzel, R.P., Bottke, W.F., Bowles, N.E., Campins, H., Clark, B.C., Clark, B.E., Connolly, H.C., Daly, M.G., de Leon, J., Delbo, M., Deshapriya, J.D.P., Elder, C.M., Fornasier, S., Hergenrother, C.W., Howell, E.S., Jawin, E.R., Kaplan, H.H., Kareta, T.R., Le Corre, L., Li, J.-Y., Licandro, J., Lim, L.F., Michel, P., Molaro, J., Nolan, M.C., Pajola, M., Popescu, M., Garcia, J.L.R., Ryan, A., Schwartz, S.R., Shultz, N., Siegler, M.A., Smith, P.H., Tatsumi, E., Thomas, C.A., Walsh, K.J., Wolner, C.W.V., Zou, X.-D., Lauretta, D.S., 2019. Properties of Rubble-Pile Asteroid (101955) Bennu from OSIRIS-REx imaging and thermal analysis. Nat. Astron. 3 (4), 341–351.

Durda, D.D., Chapman, C.R., Cintala, M.J., Flynn, G.J., Strait, M.M., Minnick, A., 2011. Experimental investigation of the impact fragmentation of blocks embedded in regolith. Meteorit. Planet. Sci. 46, 149–155.

Güttler, C., Hirata, N., Nakamura, A.M., 2012. Cratering experiments on the self armoring of coarse-grained granular targets. Icarus 220, 1040–1049.

Hirata, N., Barnouin-Jha, O.S., Honda, C., Nakamura, R., Miyamoto, H., Sasaki, S., Demura, H., Nakamura, A.M., Michikami, T., Gaskell, R.W., Saito, J., 2009. A survey of possible impact structures on 25143 Itokawa. Icarus 200, 486–502.

Holsapple, K.A., Housen, K.R., 2012. Momentum transfer in asteroid impacts. I. Theory and scaling. Icarus 221, 875–887.

Holsapple, K.A., Schmidt, R.M., 1987. Point source solutions and coupling parameters in cratering mechanics. J. Geophys. Res. 92 (B7), 6350–6376.

Housen, K.R., Holsapple, K.A., 2011. Ejecta from impact craters. Icarus 211 (1), 856–875.

Housen, K.R., Holsapple, K.A., 2014. Momentum transfer during impacts into rocky rubble-pile asteroids. In: Lunar and Planetary Science Conference, vol. 45, p. 2528.

Housen, K.R., Sweet, W.J., Holsapple, K.A., 2018. Impacts into porous asteroids. Icarus 300, 72–96.

Jutzi, M., Michel, P., 2014. Hypervelocity impacts on asteroids and momentum transfer I. Numerical simulations using porous targets. Icarus 229, 247–253.

Jutzi, M., Benz, W., Michel, P., 2008. Numerical simulations of impacts involving porous bodies: I. implementing sub-resolution porosity in a 3D SPH hydrocode. Icarus 198 (1), 242–255.

Jutzi, M., Michel, P., Benz, W., Richardson, D.C., 2010. Fragment properties at the catastrophic disruption threshold: the effect of the parent body's internal structure. Icarus 207 (1), 54–65.

Jutzi, M., 2015. SPH calculations of asteroid disruptions: the role of pressure dependent failure models. Planet. Space Sci. 107, 3–9. VIII Workshop on Catastrophic Disruption in the Solar System.

Kadono, T., Suetsugu, R., Arakawa, D., Kasagi, Y., Nagayama, S., Suzuki, A.I., Hasegawa, S., 2019. Pattern of impact-induced ejecta from granular targets with large inclusions. Astrophys. J. Lett. 880, L30. https://doi.org/10.3847/2041-8213/ab303f.

Lauretta, D.S., DellaGiustina, D.N., Bennett, C.A., Golish, D.R., Becker, K.J., Balram-Knutson, S.S., Barnouin, O.S., Becker, T.L., Bottke, W.F., Boynton, W.V., Campins, H., Clark, B.E., Connolly, H.C., d'Aubigny, C.Y.D., Dworkin, J.P., Emery, J.P., Enos, H.L., Hamilton, V.E., Hergenrother, C.W., Howell, E.S., Izawa, M.R.M., Kaplan, H.H., Nolan, M.C., Rizk, B., Roper, H.L., Scheeres, D.J., Smith, P.H., Walsh, K.J., Wolner, C.W.V., 2019. The unexpected surface of asteroid (101955) Bennu. Nature 568 (7750), 55.

Luther, R., Zhu, M.-H., Collins, G.S., Wünnemann, K., 2018. Effect of target properties and impact velocity on ejection dynamics and ejecta deposition. Meteorit. Planet. Sci. 53 (8), 1705–1732.
Melosh, H.J., 1989. Impact Cratering: a Geologic Process. Oxford Monographs on Geology and Geophysics. Oxford University Press. 245 pp.
Melosh, H.J., 2007. A hydrocode equation of state for SiO2. Meteorit. Planet. Sci. 42, 2079–2098.
Michel, P., Kueppers, M., Sierks, H., Carnelli, I., Cheng, A.F., Mellab, K., Granvik, M., Kestilä, A., Kohout, T., Muinonen, K., Näsilä, A., Penttila, A., Tikka, T., Tortora, P., Ciarletti, V., H´ erique , A., Murdoch, N., Asphaug, E., Rivkin, A., Barnouin, O., Bagatin, A.C., Pravec, P., Richardson, D.C., Schwartz, S.R., Tsiganis, K., Ulamec, S., Karatekin, O., 2018. European component of the AIDA mission to a binary asteroid: characterization and interpretation of the impact of the DART mission. Adv. Space Res. 62 (8), 2261–2272.
Michikami, T., Honda, C., Miyamoto, H., Hirabayashi, M., Hagermann, A., Irie, T., Nomura, K., Ernst, C.M., Kawamura, M., Sugimoto, K., Tatsumi, E., Morota, T., Hirata, Naru, Noguchi, T., 2019. Boulder size and shape distributions on asteroid Ryugu. Icarus 331, 179–191.
Mizutani, H., Kawakami, S.-I., Takagi, Y., Kumazawa, M., Kato, M., 1983. Cratering experiments in sands and a trial for general scaling law. In: Lunar and Planetary Science Conference Proceedings, vol. 88, pp. 835–845.
Ormö, J., Melero-Asensio, I., Housen, K.R., Wünnemann, K., Elbeshausen, D., Collins, G.S., 2015. Scaling and reproducibility of craters produced at the Experimental Projectile Impact Chamber (EPIC), Centro de Astrobiologia Spain. Meteorit. Planet. Sci. 50 (12), 2067–2086.
Piekutowski, A.J., 1977. Cratering mechanisms observed in laboratory-scale high-explosive experiments. In: Impact and Explosion Cratering: Planetary and Terrestrial Implications, pp. 67–102.
Piekutowski, A.J., 1980. Formation of bowl-shaped craters. In: Lunar and Planetary Science Conference Proceedings, vol. 3, pp. 2129–2144.
Popova, O., Borovička, J., Hartmann, W.K., Spurný, P., Gnos, E., Nemtchinov, I., Trigo-Rodriguez, J.M., 2011. Very low strengths of interplanetary meteoroids and small asteroids. Meteorit. Planet. Sci. 46, 1525–1550.
Quaide, W.L., Oberbeck, V.R., 1968. Thickness determinations of the lunar surface layer from lunar impact craters. J. Geophys. Res. 73 (16), 5247–5270.
Raducan, S.D., Jutzi, M., 2022. Global-scale reshaping and resurfacing of asteroids by small-scale impacts, with applications to the DART and Hera missions. Planet. Sci. J. 3, 128.
Raducan, S.D., Davison, T.M., Luther, R., Collins, G.S., 2019. The role of asteroid strength, porosity and internal friction in impact momentum transfer. Icarus 329, 282–295.
Raducan, S.D., Davison, T.M., Collins, G.S., 2020. The effects of asteroid layering on ejecta mass-velocity distribution and implications for impact momentum transfer. Planet. Space Sci. 180, 104756.
Richardson, D.C., Leinhardt, Z.M., Melosh, H.J., Bottke Jr., W.F., Asphaug, E., 2002. Gravitational aggregates: evidence and evolution. In: Asteroids III, pp. 501–515.
Rozitis, B., MacLennan, E., Emery, J.P., 2014. Cohesive forces prevent the rotational breakup of rubble-pile asteroid (29075) 1950 DA. Nature 512, 174–176.
Sánchez, P., Scheeres, D.J., 2014. The strength of regolith and rubble pile asteroids. Meteorit. Planet. Sci. 49, 788–811.
Schmidt, R.M., Housen, K.R., 1987. Some recent advances in the scaling of impact and explosion cratering. Int. J. Impact Eng. 5 (1–4), 343–355.
Schultz, P.H., Gault, D.E., 1985. Clustered impacts: experiments and implications. J. Geophys. Res. 90, 3701–3732.
Tatsumi, E., Sugita, S., 2018. Cratering efficiency on coarse-grain targets: implications for the dynamical evolution of asteroid 25143 Itokawa. Icarus 300 (227), 248.
Walsh, K.J., Jawin, E.R., Ballouz, R.-L., Barnouin, O.S., Bierhaus, E.B., Connolly, H.C., Molaro, J.L., McCoy, T.J., Delbo', M., Hartzell, C.M., Pajola, M., Schwartz, S.R., Trang, D., Asphaug, E., Becker, K.J., Beddingfield, C.B., Bennett, C.A., Bottke, W.F., Burke, K.N., Clark, B.C., Daly, M.G., DellaGiustina, D.N., Dworkin, J.P., Elder, C.M., Golish, D.R., Hildebrand, A.R., Malhotra, R., Marshall, J., Michel, P., Nolan, M.C., Perry, M.E., Rizk, B., Ryan, A., Sandford, S.A., Scheeres, D.J., Susorney, H.C.M., Thuillet, F., Lauretta, D.S., 2019. Craters, boulders and regolith of (101955) Bennu indicative of an old and dynamic surface. Nat. Geosci. 130 (12). 4. p. 242.
Zhang, Y., Michel, P., Richardson, D.C., Barnouin, O.S., Agrusa, H.F., Tsiganis, K., Manzoni, C., May, B.H., 2021. Creep stability of the DART/Hera mission target 65803 Didymos: II. The role of cohesion. Icarus 362, 114433.